Mon. Not. R. Astron. Soc. **283,** 282–296 (1996)

# Host galaxies of intermediate redshift radio-loud and radio-quiet quasars

Jari Rönnback,[1,2] Ernst van Groningen,[2] Ignaz Wanders[3] and Eva Örndahl[2]

[1]*European Southern Observatory, Karl-Schwarzschild-Strasse 2, D-85748 Garching bei München, Germany*
[2]*Astronomiska observatoriet, Box 515, S-751 20 Uppsala, Sweden*
[3]*Department of Astronomy, Ohio State University, 174 West 18th Avenue, Columbus, OH 43210, USA*

Accepted 1996 June 30. Received 1996 June 17; in original form 1995 November 30

## ABSTRACT

In a search for host galaxies associated with quasars, we present results from deep CCD imaging using the European Southern Observatory (ESO) 3.5-m New Technology Telescope (NTT). 21 targets, 12 radio-loud and nine radio-quiet quasars, were observed in $R$, and additional $V$ and Gunn $i$ images were collected for a subgroup of these. The quasar redshifts are between 0.4 and 0.8, a range largely unexplored in previous studies. At these redshifts the $R$ band corresponds to a rest-frame wavelength between 4600 and 3600 Å. Thus, we are primarily probing the light from young stellar components of the presumed host galaxies. To separate out the light originating from the host object we remove the quasar contribution by scaling the point spread function (PSF). The PSF is a combination of an empirical PSF model, derived from stars lying in the same field as the quasars (used for the core of the PSF), and an analytical model for the wings of the PSF.

After PSF subtraction of the QSO image we identify extended residual objects in 17 targets (nine in radio-loud and eight in radio-quiet quasars), of which a few are only marginal detections. These objects are large and luminous and their colours are relatively blue. Their $V-R$ colours are consistent with a stellar population typical of late-type spirals and irregular galaxies. This is true even for the hosts which were best fitted by an elliptical-type luminosity profile. The blue colours could be caused by recent star formation events or by scattering of the QSO light. The luminosity profiles of the hosts in radio-loud quasars are preferentially fitted with elliptical $r^{1/4}$ models, while the luminosity profiles of the hosts in radio-quiet quasars either are of the elliptical type or are exponential discs. We argue that stars in the host galaxy are the main source of the extended emission.

The mean value of the absolute $R$ magnitude is $-22.3 \pm 0.2$ for the hosts of the radio-loud quasars and $-22.0 \pm 0.2$ for the hosts of the radio-quiet quasars. In two cases where no extended light source was found, the limiting magnitudes are $\lesssim -20.0$.

Close companion galaxies and signs of tidal forces are found to be a common feature.

**Key words:** galaxies: photometry – quasars: general.

## 1 INTRODUCTION

In those cases in which the host galaxy of a radio-loud quasar (RLQ) is unambiguously detected, it is generally found to be of earlier morphological type, $\sim 0.5$–1 mag brighter and more extended than the hosts of radio-quiet quasars (RQQ) (Smith et al. 1986; Véron-Cetty & Woltjer 1990; Hutchings & Neff 1992). This is in analogy with objects at lower redshifts, where radio galaxies are found in ellipticals, while Seyferts lie in spiral galaxies (MacKenty 1990). On this basis it has been speculated that the radio galaxies are the faded remnants of radio-loud quasars.

These observed circumstances suggest that there is a connection between the processes that ultimately result in a certain galaxy morphology and the processes in the active centre. Understanding the nature of this connection has been one of the main motivations in studies of quasar host galaxies.

The optical to near-IR colours of the quasar host galaxies have been found to be somewhat bluer than in non-active galaxies of comparable morphologies (Véron-Cetty & Woltjer 1990; McLeod & Rieke 1994a). Hutchings, Janson & Neff (1989) find an average difference of 1.3 mag in $R$ between RLQs and RQQs, while this difference increases to 1.9 in $B$. Compact blue knots have recently been resolved, using the *Hubble Space Telescope* (*HST*), in hosts of low-redshift quasars (Hutchings & Morris 1995; Bahcall, Kirhakos & Schneider 1995). This could indicate recent star formation events.

A popular picture, qualitatively explaining some of these observed phenomena, is that interacting and merging galaxies trigger the star formation and provide the fuel for the active nucleus (see e.g. Sanders et al. 1988). The hosts of RLQs seem to be of elliptical type, which could be related to the fact that they reside in denser environments, and hence have higher merging rates (transforming spirals into ellipticals). The presumed massive black holes in the centres of these galaxies must have different properties from those in spirals. For instance, they could have a higher spin rate as a result of the interaction between two massive black holes in the merging process (Wilson & Colbert 1995). Presumably, this is a relatively rare event, thus explaining the low frequency of RLQs compared to RQQs. The interacting/merging model is supported by recent high-resolution images obtained with the *HST* (Bahcall et al. 1995; Disney et al. 1995) which reveal that close compansion galaxies are a very common feature. It is well known that there exist nearby interacting galaxies that do not have an active nucleus, however. Maybe not all low-redshift galaxies have a massive central black hole; alternatively, the quasar phenomenon at this redshift could be a less luminous event, of short duration, because most of the gas has already been consumed in star formation.

Recent studies of quasars at high redshifts, $z>1$ (Lowenthal et al. 1995; Hutchings, Crampton & Johnson 1995; Huchings 1995) have found similarities with low-redshift studies regarding the morphological properties of the hosts. The study by Hutchings et al. (1995) indicates that both RLQs and RQQs are generally found in rich environments at redshifts $>1$, containing a high fraction of star-bursting galaxies. Ellingson, Yee & Green (1991) found that the luminosity of the RLQs in rich environments fades rapidly ($\sim 4$ mag) between $z=0.6$ to 0.3, and that the environments of RQQs are sparser than for RLQs at these redshifts. These findings are consistent with the merging model discussed above.

In order to extend these studies to intermediate redshifts we have carried out a campaign in which about 100 QSOs, at $0.4<z<0.8$, have been observed with several optical filters. The colour measurements are crucial for the understanding of this type of object because they can give information on the recent star formation history. Here we present the first results from observations of 23 QSOs obtained at the European Southern Observatory (ESO) with the 3.5-m New Technology Telescope (NTT). The images have good spatial resolution (FWHM $\sim 0.5$–$0.9$ arcsec). In this paper we concentrate on the methodology of removing the QSO light from the data.

Throughout this paper we assume $q_0=0.5$ and $H_0=80$ km s$^{-1}$ Mpc$^{-1}$.

## 2 SAMPLE CRITERIA

The sample quasars were selected from the catalogues of Véron-Cetty & Véron (1993) and Hewitt & Burbidge (1993). The only selection criteria used were the redshift range, $0.4<z<0.8$, and the sky coordinates. General data assembled from the literature are shown in Table 1. The $V$ magnitudes were extracted from two sources, the extragalactic database NASA/IPAC Extragalactic Database (NED) (labelled $V_{\rm NED}$ in Table 1) and the Véron-Cetty & Véron catalogue. For three QSOs, $V$ differs by $\sim 1.5$ mag in these two catalogues; in such cases we used the values listed by Véron-Cetty & Véron. Fig. 1 shows the distribution in the absolute $V$ magnitude versus redshift diagram. The distribution in redshift and absolute luminosity is somewhat narrower for the RQQs. The classification as an RLQ or RQQ was done in terms of the 5 GHz luminosities: following Dunlop et al. (1993) we define an RLQ as having a radio flux $>10^{24}$ W Hz$^{-1}$ sr$^{-1}$. For PKS 1004−217, $\log(L_{5\,\rm GHz})=23.9$ but we still rate it as an RLQ. The upper flux limit of the quasars that do not have a registered radio flux, the radio-quiet sample QSOs, is $\log(L_{5\,\rm GHz})\sim 23.2$–$23.5$ W Hz$^{-1}$ sr$^{-1}$ (Griffith et al. 1994, 1995; Wright et al. 1994).

The rest frame wavelength corresponding to the $R$ filter is $\sim 4300$ Å (FWHM $=1111$ Å) at $z=0.5$ and $\sim 3600$ Å (FWHM $=926$ Å) at $z=0.8$. These roughly correspond to the Bessel $B$ band ($\lambda_c\sim 4340$ Å and FWHM $=1011$ Å) and Bessel $U$ band ($\lambda_c\sim 3542$ Å and FWHM $=531$ Å), respectively. The emission line [O II]$\lambda$3727, which is strong in star-forming objects and hot nebulae, lies within the filter profile at all redshifts probed. Our observations are therefore more sensitive to star-forming galaxies, which also have a bluer stellar continuum, than to galaxies with old stellar populations. Stockton & MacKenty (1987) found that about 25 per cent of their sample of 47 luminous QSOs are surrounded by extended line emission. However, the correction for the $R$ magnitude is not expected to be more than a few tenths of a magnitude (Smith et al. 1986; Romanishin & Hintzen 1989). Should the host consist of an old stellar population, a better approach is perhaps to observe in the near infrared, where the non-stellar emission from the QSO also is relatively fainter, as was done e.g. in the studies by Véron-Cetty & Woltjer (1990), Dunlop et al. (1993) and McLeod & Rieke (1994a,b).

All optical magnitudes have been corrected for the galactic extinction (Burstein & Heiles 1982), given in Table 1.

## 3 OBSERVATIONS AND DATA REDUCTIONS

The data were obtained, during excellent atmospheric conditions, in 1994 January at ESO with the 3.5-m NTT, equipped with the Superb Seeing Imager (SUSI). The pixel size of the TEK $1024^2$ CCD at SUSI is $0.13\times 0.13$ arcsec$^2$.

**Table 1.** General properties and observation summary of the sample quasars. $M_V$ and $L_{5\,GHz}$ were derived assuming $H_0=80$ km s$^{-1}$ Mpc$^{-1}$ and $q_0=0.5$. Ext($B$) is the galactic extinction in the $B$ band. The integration times are for the $R$, $V$ and $i$ bands, respectively. The seeing FWHM values pertain to the $R$ band.

| Object | $\alpha_{1950}$ ($h$ $m$ $s$) | $\delta_{1950}$ ($^\circ$ $'$ $''$) | z | $V$ | $V_{NED}$ | Ext($B$) | $M_V$ | log($L_{5GHZ}$) (W Hz$^{-1}$ sr$^{-1}$) | Int. time (s) $R$ | $V$ | $i$ | FWHM (arcsec) |
|---|---|---|---|---|---|---|---|---|---|---|---|---|
| PKS | 02 52 00 | -54 54 02 | 0.537 | 18.0 | 19.3 | 0.02 | -23.7 | 24.5 | 1200 | | | 0.7 |
| 0314-380 | 03 14 19 | -38 01 43 | 0.484 | | 17.3 | 0.00 | -24.2 | | 1800 | | | 0.7 |
| 0333-343 | 03 33 43 | -34 17 44 | 0.621 | | 18.1 | 0.00 | -24.0 | | 1800 | 1200 | 600 | 0.7 |
| E | 03 42 52 | -25 01 41 | 0.653 | | 18.8 | 0.00 | -23.4 | | 1200 | 1200 | | 0.7 |
| PKS | 04 03 14 | -13 16 18 | 0.571 | | 17.2 | 0.10 | -24.7 | 25.1 | 1200 | 1200 | 1200 | 0.5 |
| 3C 110 | 04 14 49 | -06 01 04 | 0.781 | | 15.9 | 0.13 | -26.7 | 24.4 | 1200 | | | 0.9 |
| MC | 04 15 06 | -20 02 10 | 0.604 | 19.5 | 19.5 | 0.05 | -22.5 | | 1800 | | | 0.7 |
| PKS | 09 20 48 | -39 46 43 | 0.591 | 18.8 | 18.8 | - | -23.2 | 24.8 | 1200 | | | 0.8 |
| PKS | 09 28 18 | 00 48 13 | 0.505 | 19.5 | 19.5 | 0.08 | -22.1 | 24.0 | 2400 | | | 0.8 |
| PKS | 09 32 43 | 02 17 40 | 0.652 | 17.4 | 17.4 | 0.11 | -24.8 | 24.3 | 1800 | | | 0.8 |
| MC | 09 46 45 | -19 43 10 | 0.519 | 17.9 | 17.5 | 0.13 | -23.8 | | 1800 | 1200 | | 0.6 |
| PKS | 09 58 02 | -04 13 08 | 0.497 | 17.8 | 18.1 | 0.06 | -23.8 | | 1200 | 600 | 600 | 0.9 |
| PKS | 10 04 25 | -21 44 44 | 0.330 | | 16.9 | - | -23.7 | 23.9 | 1800 | 500 | | 0.7 |
| 1016-028 | 10 16 29 | -02 48 47 | 0.717 | 18.5 | 18.5 | 0.04 | -23.9 | | 1800 | | | 0.6 |
| 1023-016 | 10 23 27 | -01 35 03 | 0.738 | 18.6 | 18.6 | 0.08 | -23.9 | | 2400 | 1200 | 1200 | 0.6 |
| 1025+023 | 10 25 11 | 02 18 46 | 0.745 | 18.6 | 18.6 | 0.08 | -23.7 | | 1800 | | | 0.7 |
| 1045-188 | 10 45 40 | -18 53 44 | 0.595 | 18.5 | 18.8 | 0.09 | -23.5 | 24.7 | 1200 | 1200 | 1200 | 0.6 |
| PKS | 11 16 06 | -46 17 50 | 0.713 | 17.0 | 17.0 | 0.58 | -25.4 | 25.0 | 1200 | | | 0.9 |
| PKS | 11 43 55 | -28 42 38 | 0.45 | 18.5 | 20.0 | 0.21 | -22.8 | 24.2 | 1200 | | | 0.8 |
| PKS | 11 56 38 | -22 11 55 | 0.565 | 20.0 | 19.5 | 0.14 | -21.8 | 24.5 | 1200 | 1200 | 600 | 0.8 |
| PKS | 12 02 59 | -26 17 22 | 0.790 | 20.0 | 19.5 | 0.49 | -22.7 | 24.9 | 1200 | | | 0.8 |

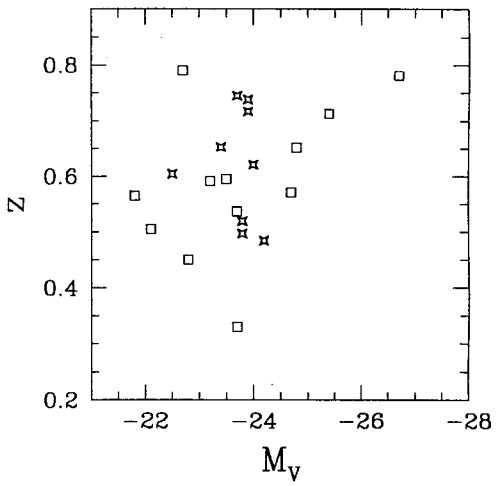


**Figure 1.** Redshift and absolute $V$ magnitudes of the radio-loud (squares) and radio-quiet quasars (stars).

The unvignetted field of view is 2.2 × 2.2 arcmin$^2$. The integration times in $R$ were typically betwen 1200 to 1800 s, split into two or three separate exposures to account for hot pixels. A record of the integration times is given in Table 1. The raw frames were checked, directly at the telescope, for fuzzy images around the quasars. For 10 objects for which we suspected that there was a host galaxy, we also obtained images in $V$ and Gunn $i$. During the complete run (3 nights) the weather was stable and photometric. The seeing varied between 0.5–0.9 arcsec, as shown in Table 1.

The flat fields in $R$ were extracted from 25 object frames which had no apparent overlapping bright objects, following the same strategy as Turner et al. (1993). The ratio of the root mean square (rms) to the mean intensity of the sky, $\sigma_{sky}/I_{sky}$, and the overall quality were found to be most favourable in the fourth-rank image of the stack of 25 images. In the median (rank 12) flat field, $\sigma_{sky}/I_{sky}$ was 2 per cent higher and it also contained a small residual structure (at the 1 per cent level of the normalized flat field). The latter was caused by the limited offset we used for the QSO image on the chip between successive exposures, which resulted in overlap in the wings of the QSO images. In $V$ and $i$ we used sky flats because the signal-to-noise ratio in the flat fields derived from object frames was too low. However, we used these to extract a large scale gradient at the 2 per cent level. Absolute flux calibration was obtained by observing standard stars from the list of Graham (1982). The Gunn $i$ magnitudes for the standards were calculated using the relations in Bessel (1979) and Wade et al. (1979).

Two other QSOs were observed but not used: PKS 0439 − 433, which overlaps with the image of a foreground spiral galaxy with $R=18.2$, and PKS 0903 − 574, which appears to be a mis-identification. In four of the brightest QSO images (0314 − 380, PKS 0403 − 133, 0414 − 060 and PKS 1004 − 217), a few central pixels were saturated.

## 4 HOST GALAXY RETRIEVAL

### 4.1 Point spread function

All object frames contain at least one unsaturated star, of comparable magnitude to the QSO, which we used as a model for the point spread function (PSF). Since the isoplanatic patch is considerably smaller than the typical separation between the stars and the QSO, we need to check if the PSF is varying significantly over the 2.2 × 2.2 arcmin$^2$ field. Two of the QSO fields (PKS 0903 − 574 and PKS 0920 − 397) are crowded with stars, and we used these to

measure the extent to which the PSF varies across the chip. Azimuthally averaged luminosity profiles were extracted from normalized and sky-subtracted images of the stars. Using three and five stars scattered over the CCD in the two different fields, we find that their luminosity profiles differ by less than 2 per cent at any radial position, over a range of 8 mag or out to a radius of 3 FWHM. Thus, the PSF does not vary significantly over the field in our frames. However, we cannot exclude the possibility that the PSF varies more in the other frames. In the images with slightly elongated point sources, the elongation is constant over the full frames.

As a first approximation we used, for each frame, the intensity-weighted median image of the stellar images as a model PSF. It turns out that the signal-to-noise ratio is often unacceptably low in the wings of the profiles. However, we used these PSFs to extract the azimuthally averaged luminosity profiles. These, together with the profiles of the QSOs, are shown in Figs 2(a) and (b). The PSFs were normalized to have the same central flux as the QSOs. In the cases in which the QSO images were saturated, the normalization was done at a radius where the CCD was not saturated and the QSO still dominated the signal. Based on these plots we detect, by visual inspection, residual light in about 60 per cent of the quasars.

To increase the accuracy of these measurements and to measure the spatial dependence of the surface brightness of the residuals, we need a better model of the two-dimensional PSF. We found that it was necessary to adopt different treatments for the core and the wings of the PSFs. In the core (where the signal-to-noise ratio is high), small tracking errors, in combination with the excellent seeing, led to a non-circular PSF, which could not be adequately modelled. In the wings, where the light profile is circular, the signal-to-noise ratio of the data can become very low. We therefore constructed a PSF using empirical data in the core and model data in the wings. We switched to model data at a radius where the contours of the empirical PSF was obviously round and before the noise started to become significant. The advantage of this approach is that no extra noise is added to the wing of the host galaxy image when we subtract the PSF from the QSO, enabling us to see fainter levels.

To model the wings of the PSFs, we used the profile discussed by Saglia et al. (1994), using a routine kindly provided by Richard Hook. This profile is characterized by

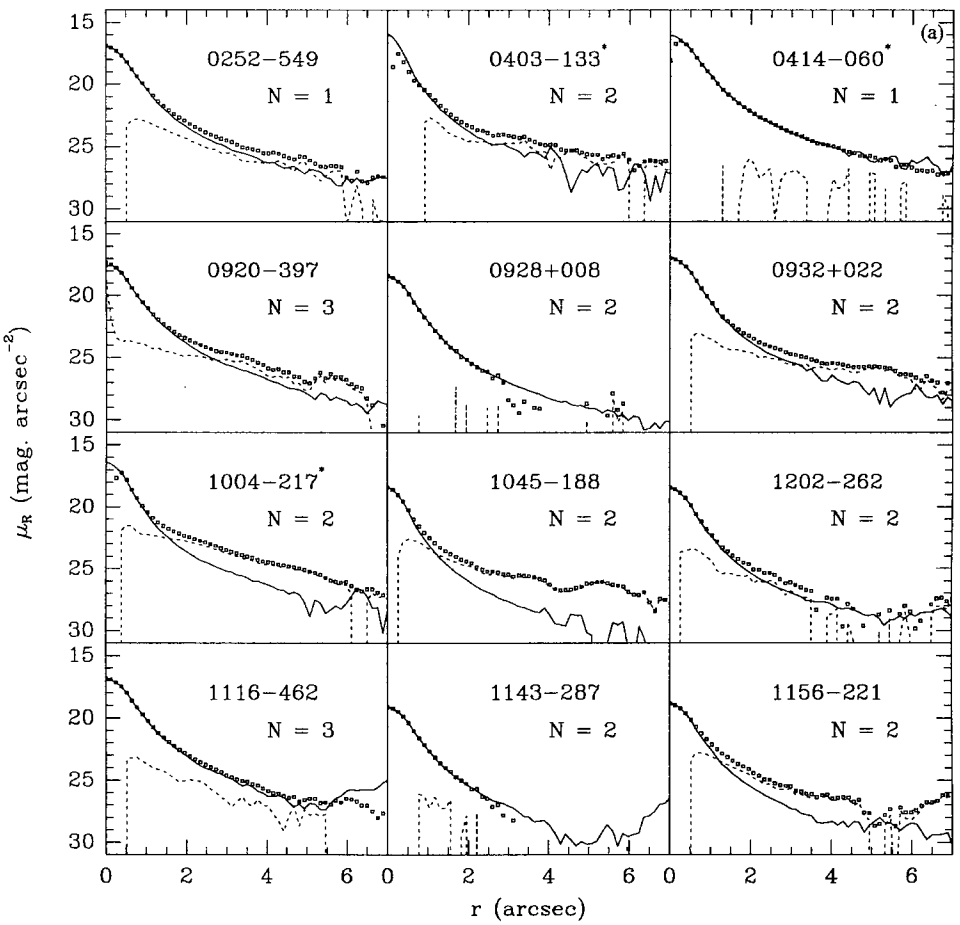


**Figure 2(a).** Azimuthally averaged luminosity profiles of the radio-loud quasars (boxes) and stellar images (solid lines) in the field of the quasars. The dashed lines show the residuals after the stellar profiles have been subtracted from the quasar profiles. *N* indicates the number of stellar objects which were used to generate the PSF profile. A star indicates that the QSO was saturated.

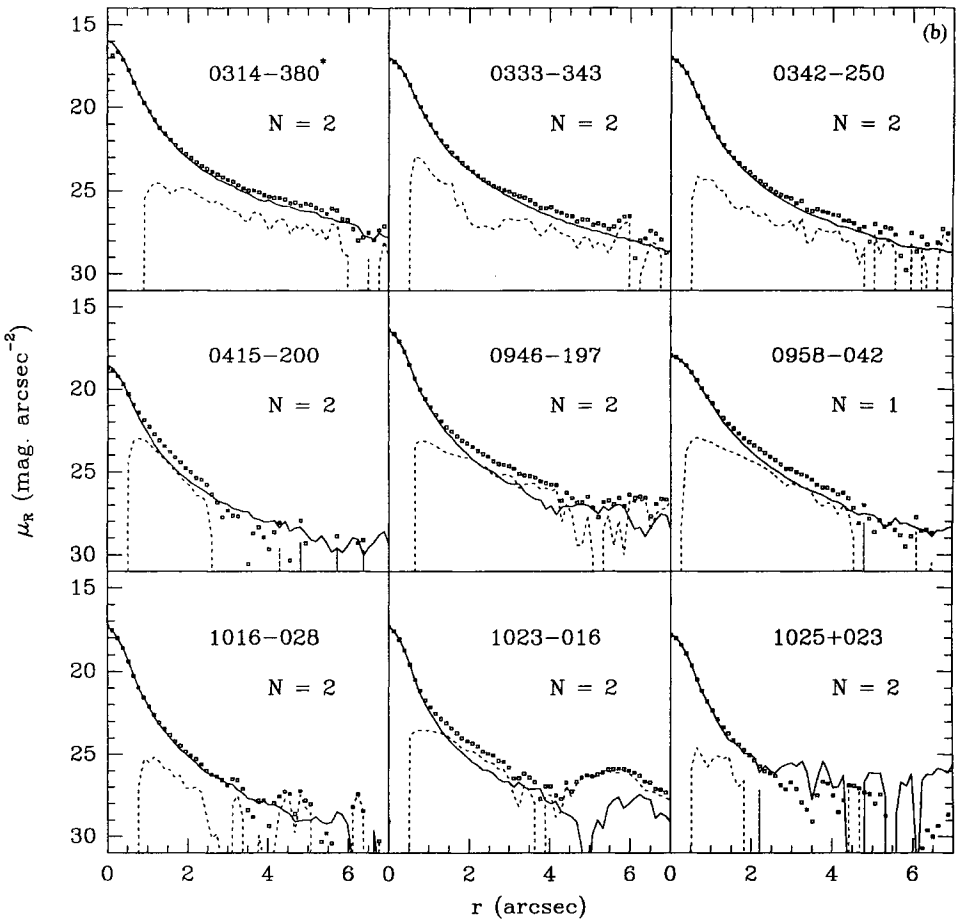


**Figure 2(b).** Same as Fig. 2(a) for the radio-quiet quasars.

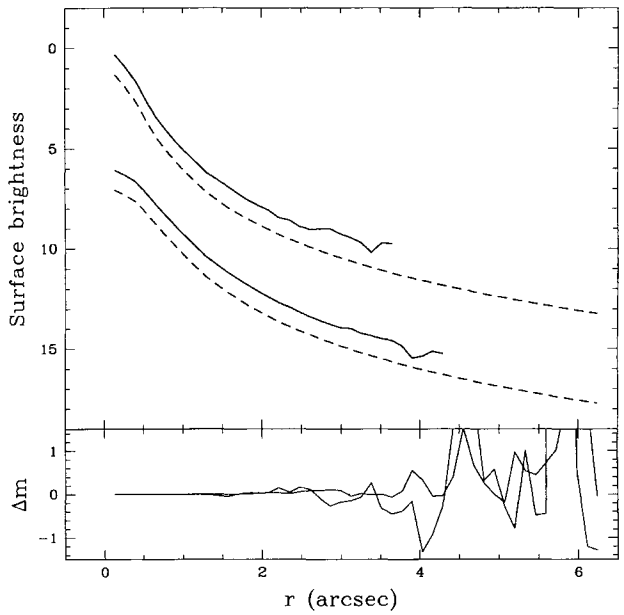


**Figure 3.** Two examples [PKS 0403 − 133, FWHM(PSF) = 0.5 arcsec (upper curves), and PKS 1116 − 462, FWHM(PSF) = 0.9 arcsec (lower curves)] of the azimuthally averaged luminosity profiles of the point spread function derived from the data (full line) and the analytical model (dashed line) discussed in the text. The *y*-axis is the surface brightness in relative units. The lower section shows the difference between the empirical and model PSFs.

a single parameter, $\gamma$, that basically sets the width of the wings. Increasing $\gamma$ yields profiles that are more peaked. For a Gaussian distribution $\gamma = 2$, while the theory of atmospheric turbulence predicts $\gamma = 5/3$. For each object we computed a grid of models, with the appropriate FWHM of the profile, varying $\gamma$ between 1.3 and 1.8 in steps of 0.02. We extracted the model profile that showed the smallest residual with the empirical PSF. The deviation of the model profile from the empirical one is less than 0.1 mag or $1-2\sigma$, within a radius of 3 − 4 FWHM. For our data we find $\gamma = 1.51 \pm 0.05$. In Fig. 3, the empirical PSF is compared to the model PSF for two cases, in which the FWHM seeing value was 0.5 and 0.9 arcsec, respectively.

Two QSO images, E 0342 − 250 and 0414 − 060, showed extended stellar spikes which could not be subtracted with the model profile. For these we used one stellar image, of approximately the same magnitude as the QSO, as a PSF. As can be seen in the contour plots (Figs 4a and b) of the QSO-subtracted images of these cases, the sky noise affects the data more than in those cases for which we used a model PSF in the wings.

### 4.2 Image restoration

As a first attempt to extract the residual two-dimensional image, we used an image-restoration technique based on a generalized Lucy–Richardson maximum entropy restora-

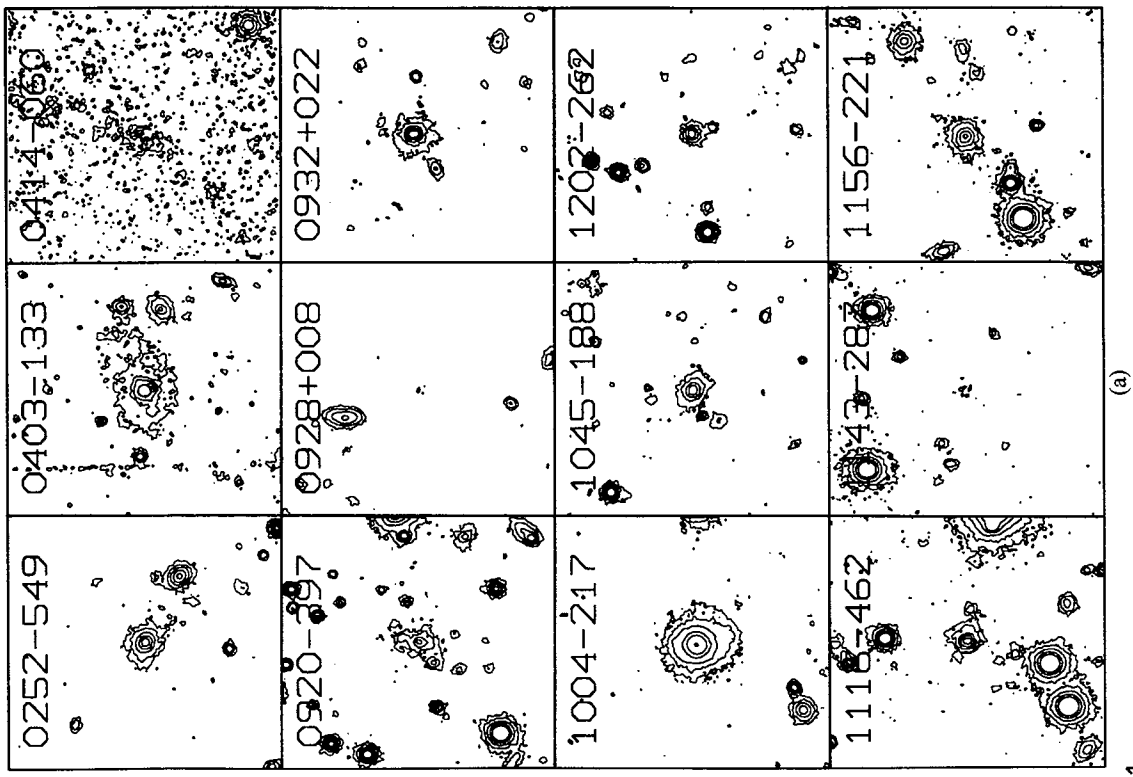


**Figure 4(a).** Contour plots of the host galaxies in radio-loud quasars showing the 21, 22, 23, 24 and 25 mag arcsec$^{-2}$ contours in *R*. Each sub-frame is 33 × 33 arcsec$^2$. The centres of the subtracted quasar images coincide with the centres of the frames. North is up and east to the left.

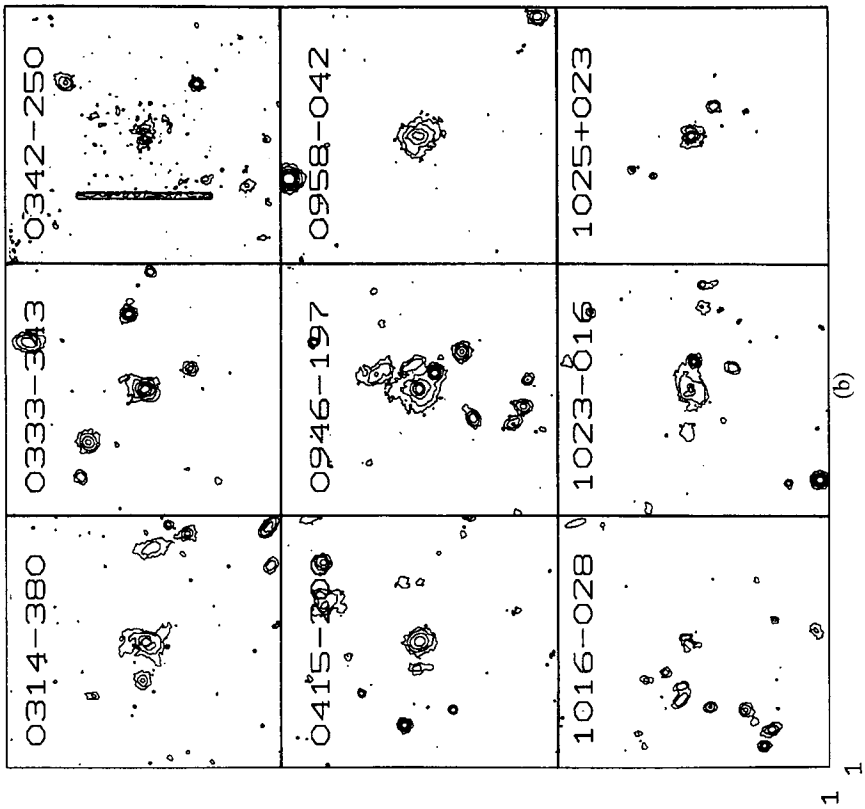


**Figure 4(b).** Same as in Fig. 4(a) for the hosts of radio-quiet quasars.

**Table 2.** Derived integrated magnitudes. The subscript *res* refers to the QSO-subtracted images. d gives the aperture, in arcsec, within which the magnitudes of the QSO-subtracted images were calculated. A colon indicates a particularly high uncertainty.

| Object | z | $R_{qso}$ | $(V-R)_{qso}$ | $(R-i)_{qso}$ | d (arcsec) | $R_{res}$ | $M_{R,res}$ | $(V-R)_{res}$ | $(R-i)_{res}$ |
|---|---|---|---|---|---|---|---|---|---|
| Radio loud quasars | | | | | | | | | |
| PKS 0252-549 | 0.537 | 17.09 | | | 0-13 | 19.36 | -22.38 | | |
| PKS 0403-133 | 0.571 | 17.03 | -0.02 | 0.04 | 3.2-13 | 19.86 | -22.02 | 0.86 | 0.46 |
| 0414-060 | 0.781 | 15.99 | | | | >20.99 | >-20.89 | | |
| PKS 0920-397 | 0.591 | 17.58 | | | 0-13 | 20.10 | -21.87 | | |
| PKS 0928+008 | 0.505 | 18.63 | | | | >21.50 | >-20.10 | | |
| PKS 0932+022 | 0.652 | 17.09 | | | 0-13 | 19.30 | -22.90 | | |
| PKS 1004-217 | 0.330 | 16.75: | 0.38: | | 3.2-13 | 19.0: | -21.77 | 0.62 | |
| 1045-188 | 0.595 | 19.19 | 0.13 | -0.01 | 0-13 | 19.96 | -22.02 | 0.91 | 0.46 |
| PKS 1116-462 | 0.713 | 16.53 | | | 0-13 | 19.40: | -23.01: | | |
| PKS 1143-287 | 0.45 | 19.08 | | | 0-13 | >21.50 | >-19.83 | | |
| PKS 1156-221 | 0.565 | 19.21 | 0.16 | 0.11 | 0-13 | 19.60 | -22.26 | 0.63 | 0.21 |
| PKS 1202-262 | 0.790 | 18.58 | | | 0-13 | 20.32: | -22.33: | | |
| Radio quiet quasars | | | | | | | | | |
| 0314-380 | 0.484 | 16.48 | | | 1.2-13 | 20.07: | -21.43: | | |
| 0333-343 | 0.621 | 17.54 | 0.03 | | 0-13 | 19.65 | -22.43 | | |
| E 0342-250 | 0.653 | 17.42 | 0.23 | | 2.6-13 | 21.24: | -20.96: | | |
| MC 0415-200 | 0.604 | 19.33 | | | 0-13 | 20.17 | -21.85 | | |
| MC 0946-197 | 0.519 | 17.19 | 0.08 | | 0-13 | 19.12 | -22.54 | 0.67 | |
| PKS 0958-042 | 0.497 | 17.82 | 0.08 | -0.67 | 0-13 | 19.96 | -21.60 | 0.71 | 1.25: |
| 1016-028 | 0.717 | 18.05 | | | | | | | |
| 1023-016 | 0.738 | 18.20 | 0.33 | -0.20 | 0-13 | 20.32 | -22.17 | 0.98 | 0.43 |
| 1025+025 | 0.745 | 18.44 | | | 0-13 | 20.97 | -21.54 | | |

tion method (Lucy 1994; Hook et al. 1994). This method is claimed to be free from the Gibbs oscillation or 'ringing' phenomenon and the tendency to flatten out peaks in the restored image, which hampered previous restoration methods. The routine divides the original image into two channels, one representing a smooth varying background (the host galaxy in our case) and another with $\delta$ functions (the QSO point source). Applying this routine to our data, we find that it has difficulty in properly allocating the contributions from the QSO and the host galaxy in the different channels, and we often end up with a restored image which has an artificial central dip in the host galaxy profile. The most likely explanation for this failure is that the cores of the host galaxies are only barely resolved. We do not present the results for this algorithm here. Instead, we concentrate on the results derived from direct subtraction of a scaled PSF from the QSO image.

### 4.3 PSF scaling

To obtain the image of the host galaxy, a properly scaled model PSF must be subtracted from the object frames. The problem here is, of course, that we do not know the QSO flux a priori. One possible way to solve this problem is to adopt the results from the image-restoration program, described above, and rescale the restored QSO flux until we get a residual image that shows a luminosity profile that decreases monotonically with radius. This method could result in oversubtraction of the QSO light, if the host galaxy profile is very peaked (as, e.g., in ellipticals and spirals with a bulge). Therefore we should regard the derived magnitudes as upper limits. Hence, the flux derived from the image-restoration program was generally reduced by a factor of about 5–10 per cent. The normalized PSF was then scaled accordingly and subtracted from the QSO. Thereafter the azimuthally averaged luminosity profile was extracted from the residual image, after removal of bright sources in the vicinity. The position angle and inclination used were the mean values derived from data having a surface brightness between 23–26 mag arcsec$^{-2}$. The measured variations in these parameters are in all cases quite modest, $\pm 10$ degrees. If the extracted profile was not decreasing monotonically with radius, we rescaled the PSF and repeated the procedure until the profile did so. Although this method of deriving the residual image of the host galaxy is subjective, it has been frequently used. For example, Disney et al. (1995) used a simlar method to derive what they refer to as 'a rough residual image of the host'. The resulting profile was fitted in a least-squares manner to a de Vaucouleurs $r^{1/4}$ law and to an exponential disc (cf. Section 4.4). We extract the structural parameters of the host galaxy from the best fit as derived from the $\chi^2$ value. Resulting magnitudes are listed in Table 2 and structural parameters in Table 3.

### 4.4 Reliability of the method

In this section we discuss how accurately we can reproduce the shape and the flux of the host galaxies. In the central parts, the profiles are affected by the procedure to remove the QSO source. For example, if the QSO flux is overestimated, a host galaxy which in reality has a peaked profile could be confused with an exponential disc. Moreover, errors in the subtraction of the sky background could force

**Table 3.** Derived structural parameters. Cases best fitted with a $r^{1/4}$ law and an exponential disc are indicated by profile types E and S, respectively. A question mark indicates that E- and S-type profiles yielded more or less equal $\chi^2$, or that the host is very faint. $P$ is the ratio between the $\chi^2$ values derived from the $r^{1/4}$ and exponential disc models. $i$ is the measured inclination and PA the position angle, as defined in the text. $r_e$ is the effective radius or scalelength of the best fit. $R^{Comp}$ is the magnitude and $d^{Comp}$ the distance to the nearest companion object. $M_R^{Comp}$ was calculated assuming that the companion has the same redshift as the QSO. The last column indicates whether there are other companion objects of comparable magnitudes and distances in the field around the QSO.

| Object | z | $i$ (degree) | PA (degree) | Type | P | $r_e$ (arcsec) | $r_e$ (kpc) | $R^{Comp}$ | $M_R^{Comp}$ | $d^{Comp}$ (kpc) | other |
|---|---|---|---|---|---|---|---|---|---|---|---|
| Radio loud quasars | | | | | | | | | | | |
| PKS 0252-549 | 0.537 | 32 | 70 | E | 0.09 | 0.78 | 3.6 | 19.9 | -21.8 | 44 | no |
| PKS 0403-133 | 0.571 | 26 | 135 | S? | 1.35 | 2.88 | 13.5 | 20.8 | -21.1 | 50 | yes |
| PKS 0920-397 | 0.591 | 56 | 170 | E? | 0.31 | 4.91 | 23.2 | 22.3 | -19.6 | 15 | yes |
| PKS 0932+022 | 0.652 | 26 | 20 | E | 0.29 | 1.58 | 7.7 | 22.0 | -20.2 | 26 | no |
| PKS 1004-217 | 0.330 | 37 | 25 | S | 11.1 | 1.33 | 4,2 | 20.5 | -20.1 | 58 | no |
| 1045-188 | 0.595 | 35 | 60 | E | 0.07 | 1.00 | 4.1 | 22.7 | -19.2 | 25 | yes |
| PKS 1116-462 | 0.713 | 26 | 100 | E | 0.16 | 0.48 | 2.4 | 21.3 | -21.1 | 66 | yes |
| PKS 1156-221 | 0.565 | 34 | 60 | E | 0.11 | 0.78 | 3.6 | 20.3 | -21.5 | 68 | yes |
| PKS 1202-262 | 0.790 | 18 | 120 | E? | 0.31 | 0.43: | 2.2 | 22.2 | -20.4 | 38 | no |
| Radio quiet quasars | | | | | | | | | | | |
| 0314-380 | 0.484 | 18 | 160 | E? | 0.36 | 1.89 | 8.3 | 22.1 | -19.4 | 23 | no |
| 0333-343 | 0.621 | 32 | 160 | E | 0.30 | 0.36 | 1.7 | 22.3 | -19.8 | 30 | yes |
| MC 0415-200 | 0.604 | 32 | 30 | S | 21.9 | 0.47 | 2.2 | 22.6 | -19.4 | 17 | no |
| MC 0946-197 | 0.519 | 35 | 55 | E? | 0.70 | 1.22 | 5.5 | 21.6 | -20.0 | 14 | yes |
| PKS 0958-042 | 0.497 | 35 | 40 | S | 2.00 | 0.77 | 3.4 | | | 8 | no |
| 1023-016 | 0.738 | 56 | 110 | S? | 2.28 | 1.12 | 5.7 | 22.8 | -19.7 | 28 | yes |
| 1025+023 | 0.745 | 32 | 90 | S? | 1.14 | 0.55 | 2.8 | 22.8 | -19.8 | 24 | no |

the exponential disc profile to resemble the elliptical $r^{1/4}$ profile. Apart from this, the PSF is actually varying (although at a low level) over the QSO field, which introduces further complications.

To estimate the accuracy of our method we have used artificial data to test the procedure in Section 4.3. First we created circular galaxy images with the luminosity profiles

$$\Sigma(r)=\Sigma(0)\exp\left[\left(\frac{r}{r_e}\right)^{-1/\beta}\right],$$

where $\Sigma(0)$, is the central surface brightness, $r$ is the radius and $r_e$ is the effective radius or scalelength of the model. The profile shape is set by the $\beta$ parameter. Here we use $\beta=4$ which is the de Vaucouleurs $r^{1/4}$ profile, applicable to early-type galaxies, and $\beta=1$, the exponential disc profile. The images were convolved with a PSF which was one of the analytical models discussed in Section 4.1. To simulate the QSO we then added a stellar image, including the sky background in the $R$ band, on top of the model galaxy. From this result we then subtracted a tilted plane representing the sky level. The standard deviations of the data points which were used to calculate the sky level (median values of the data collected in a number of boxes ($\sim 25$ pixel a side) covering a $\sim 35 \times 35$ arcsec$^2$ region around the object) corresponds to $\sim 28$ mag arcsec$^{-2}$. Thus, uncertainties in the sky background will not be the dominant error because we do not use data with surface brightness less than $\sim 27$ mag arcsec$^{-2}$, as described below. To derive images comparable to our host galaxy images, we then subtracted a model PSF from the result, in the same manner as in the previous section. The stellar image used for the central part of the final model PSF was different from the stellar image which was used to simulate the QSO, but they were extracted from the same data frame.

To cover the range of observing conditions and expected properties of the host galaxies, we ran 36 simulations with different PSFs and structural parameters of the galaxy models. We used two different data sets; one with a FWHM of the PSF of 0.6 arcsec and a QSO magnitude of 17.4, and the other with 0.8 arcsec and a QSO magnitude of 18.6. These QSO fluxes are typical for our data. The effective radii of the $r^{1/4}$ and disc models were the same; 0.5, 1.0 and 1.5 arcsec. For each of these we constructed models with galaxy magnitudes of 19, 20 and 21. The resulting azimuthally averaged luminosity profiles are shown in Fig. 5.

All profiles were least-squares fitted to both the $r^{1/4}$ and the disc models, and we computed the ratio of the $\chi^2$ statistic, $P$, of the two fits. If this ratio is significantly below one, the $r^{1/4}$ models provides the best fit, and vice versa. The inner radius of the fit was set to about 6 pixels for the 0.6 arcsec PSF and 8 pixels for the 0.8 arcsec PSF. This is approximately the radius at which the original and scaled models intersect again, as seen in Fig. 5, at least for the brighter models. By repeating the fitting procedure with different outer radii, from levels corresponding to 25 down to 28 mag arcsec$^{-2}$, we find that the optimal outer radius varies from case to case. An outer radius in the range $\sim 26$–$27$ mag arcsec$^{-2}$ seems to be preferable, in terms of optimizing $P$ and reproducing the scalelength. Thus, we use an outer radius of $\sim 26.5 \pm 0.5$ mag arcsec$^{-2}$ throughout

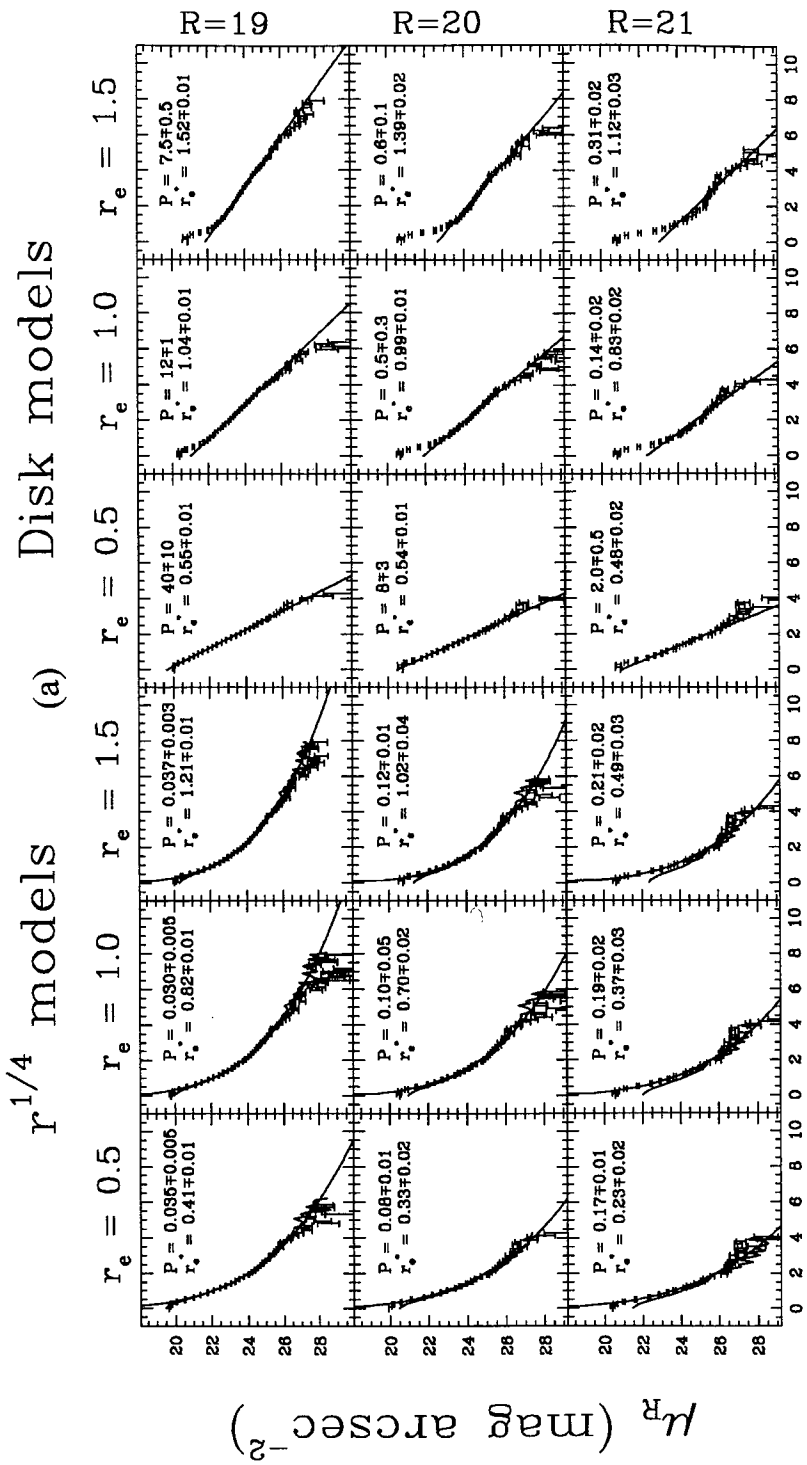


**Figure 5.** Luminosity profiles of the model host galaxies. (a) FWHM(PSF) = 0.6 arcsec and (b) FWHM(PSF) = 0.8 arcsec. Data points shows the luminosity profiles of the PSF-subtracted QSO + host model galaxies. The error bars show the $1\sigma$ deviation. Full drawn lines show the profiles of the best fits to the data. $r^{1/4}$ models are shown to the left and exponential disc to the right. The additional full-drawn line in the $r^{1/4}$ models (shown over the same range as the data points) shows the luminosity profile of the PSF-convolved model galaxy (i.e. without adding and subtracting a model QSO). The magnitudes of the galaxy models are displayed to the right of the plots and the scalesizes (in arcsec) on top of the plots. The scalesize of the best fit, $r_e^*$ is given for each case. The $P$ value, which describes how well the profile shape is reproduced, is defined in the text.

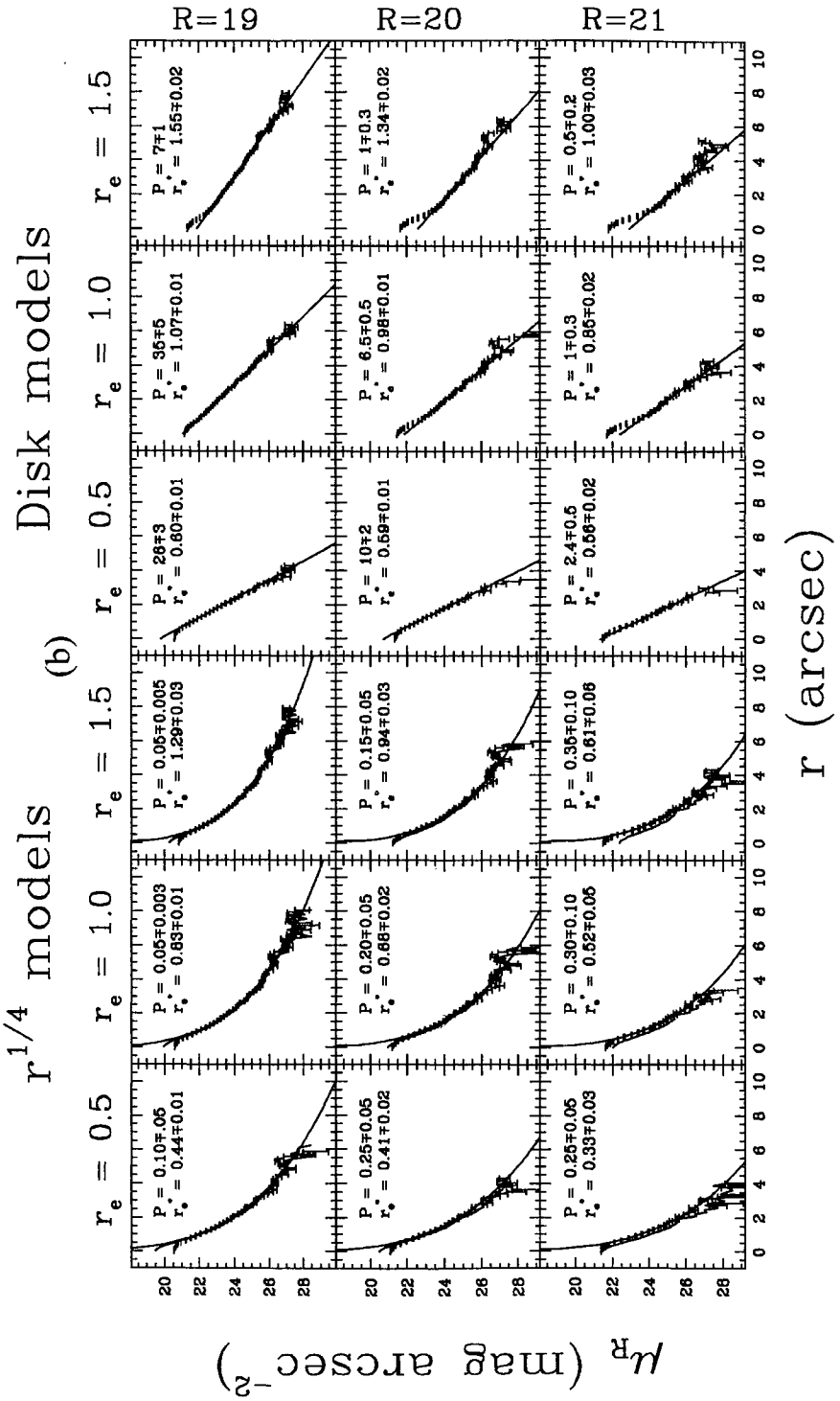


**Figure 5** – *continued*

this study. The profiles, values of $P$ and scalesizes of the best fits are shown in Fig. 5. The errors quoted in the figures show the typical deviation as the outer radius is varied between contours at a level of 26–27 mag arcsec$^{-2}$.

Except for the faintest ($R=21$) models, we can reproduce the profile shape quite well. The effective radii, for the $r^{1/4}$ models, are systematically underestimated with a factor of $\gtrsim 0.2$ if $R=19$, $\gtrsim 0.3$ if $R=20$ and $\gtrsim 1$–2 if $R=21$. This is partly due to the smoothing of the profile by the seeing, which steepens the central part of the profile. For the exponential disc the situation is better, as the scalelength is reproducible within 10–30 per cent over the whole range of parameters used here. The uncertainty, allowing for the errors in the sky subtraction ($1\sigma$), is of the order of 3, 10 and 15 per cent for the models with $R=19$, 20 and 21 mag, respectively. Compact models are easier to reproduce than more extended profiles of the same magnitude, because the latter are more affected by the sky noise. For the exponential disc models with $r_e \leq 1.0$ arcsec and $R \gtrsim 20$, $P < 1$, at least for the case in which the FWHM of the PSF is 0.6 arcsec. This is partly caused by a small difference between the two stellar images used in the modelling of the QSO and the PSF in this case. However, by increasing the inner radius by a factor of about 50 per cent, we derive $P \sim 2$ in these cases too.

We also ran a subsection of models with elongated (inclination equal to 45°) images and derived essentially the same results, also with an error in the position angle of $\pm 5°$ and inclination of $\pm 10°$. The latter values are the limits within which we can reproduce the position angle and inclination if $R \leq 20$ mag. We should allow for an extra uncertainty of about 5 per cent in the derived scalesizes because of this.

Additional possible complications, not accounted for in the models above, could be that the nuclear point source is not necessarily centred on the host galaxy and there may be small scale deviations in the luminosity profile, such as spiral arms, H II regions or tidal arm structures. If the miscentring of the QSO is less than a few pixels, as we expect, it would not change the $P$-values significantly, although the derived structural parameters would change slightly.

The observed host galaxies typically have $R \sim 20$, therefore we are quite confident that we have derived a highly probable result. The errors in the derived scalesizes we estimate to be 30–40 per cent. For the host galaxies with $P$-values in the range 0.5–1.5 or $M \gtrsim 20$, we regard the results as very tentative.

Comparing the integrated fluxes of the PSF-convolved model galaxies and the PSF-subtracted QSO + host galaxy models, we find that they differ with $0.10 \pm 0.05$, $0.20 \pm 0.10$ and $0.50 \pm 0.10$ mag when $R=19$, 20 and 21 mag, respectively. These values are comparable to the results of Maraziti & Stockton (1994) in a similar study.

As a further check of the reliability of this method we subtracted, in all cases, the two stellar images which were used to generate the PSF from each other and inspected the residual image. This resulted, in all cases, in a very inconspicuous residual (both in size and flux). However, if $M > 21.5$ we cannot reproduce any residual image after the PSF subtraction, independent of the scalesize of the model galaxy. In the two observed cases, PKS 0928 + 008 and PKS 1143 – 287, where no residual image is seen, we thus take $R=21.5$ as the lower limiting magnitude of the host.

## 5 RESULTS AND DISCUSSION

The contour plots of the QSO subtrated images are shown in Fig. 4a (RLQs) and 4b (RQQs). Residual images are definitely detected in: PKS 0252 – 549, PKS 0403 – 133, PKS 0920 – 397, PKS 0932 + 022, PKS 1004 – 217, 1045 – 188, PKS 1116 – 462 and PKS 1156 – 221 in the RLQ sample, and in 0314 – 380, 0333 – 343, MC 0415 – 200, MC 0946 – 197, PKS 0958 – 042 and 1023 – 016 for the RQQs. The signal in the luminosity profiles and the images of E 0342 – 250, PKS 1202 – 262 and 1025 + 023 indicate that we may have detected the host galaxy also in these QSOs. In 0414 – 060, PKS 0928 + 008, PKS 1143 – 287 and 1016 – 028 we do not detect a host object. In the images with the best resolution it is clear, from the inspection of the morphology of the residual image, that the source is mainly stellar emission. The alternative is that the source is scattered quasar light or nebular emission from hot gas. The colours (see Table 2), however, do not favour scattered light. They should be bluer than the QSO colour in the case of dust scattering, and identical to the QSO colour in the case of electron scattering. A glance at Table 2 shows that the colours of the hosts are much redder than the QSOs. As discussed in Section 2, the [O II]$\lambda$3727 emission line lies within the filter profile, so there is probably some contribution from this line in the $R$ bands. The residual light cannot be nebular emission only, because in that case $V$–$R$ should be extremely red (unless the nebular continuum dominates) since no strong line emission is expected in the $V$ band. Thus, our working hypothesis is that the residual light is mainly due to stellar emission from a host galaxy.

Summarizing this part we find a host galaxy in 67 per cent (75 per cent) of the RLQs and 67 per cent (89 per cent) of the RQQs, where the values in parentheses include the uncertain cases. The typical absolute $R$ magnitude is $-22.3 \pm 0.2$ for the hosts in RLQs and $-22.0 \pm 0.2$ for the hosts in RQQs. Thus, the magnitude difference is only significant at the $1.5\sigma$ level.

The luminosity profiles of the hosts are displayed in Fig. 6, where the profiles of the best fits also are shown. We note that there is no correlation between the magnitude difference of the QSO and the host, and the derived scalelengths. Neither is there any correlation between the redshifts and scalelengths.

RLQs commonly occur in elliptical-type galaxies. However, this is not exclusively the case, see e.g. PKS 1004 – 217. RQQs are found in spiral discs or in ellipticals, consistent with the recent findings by Robson et al. (1995). The metric scales of the scalelengths in elliptical (excluding PKS 0920 – 397) and disc types are $\sim 4$ and $\sim 3$ kpc, respectively, in the mean. The data for the RLQs can be compared with the study of RLQs at similar redshifts by Romanishin & Hintzen (1989). The atmospheric conditions were much poorer during their observations, however, the FWHM of the seeing profile was about twice as large as in our data. We derive profiles with similar effective radii in the mean. Their mean $R$ magnitude is $\sim 0.2$ mag fainter than the one we derive. Thus, their main conclusion, that the host galaxies of

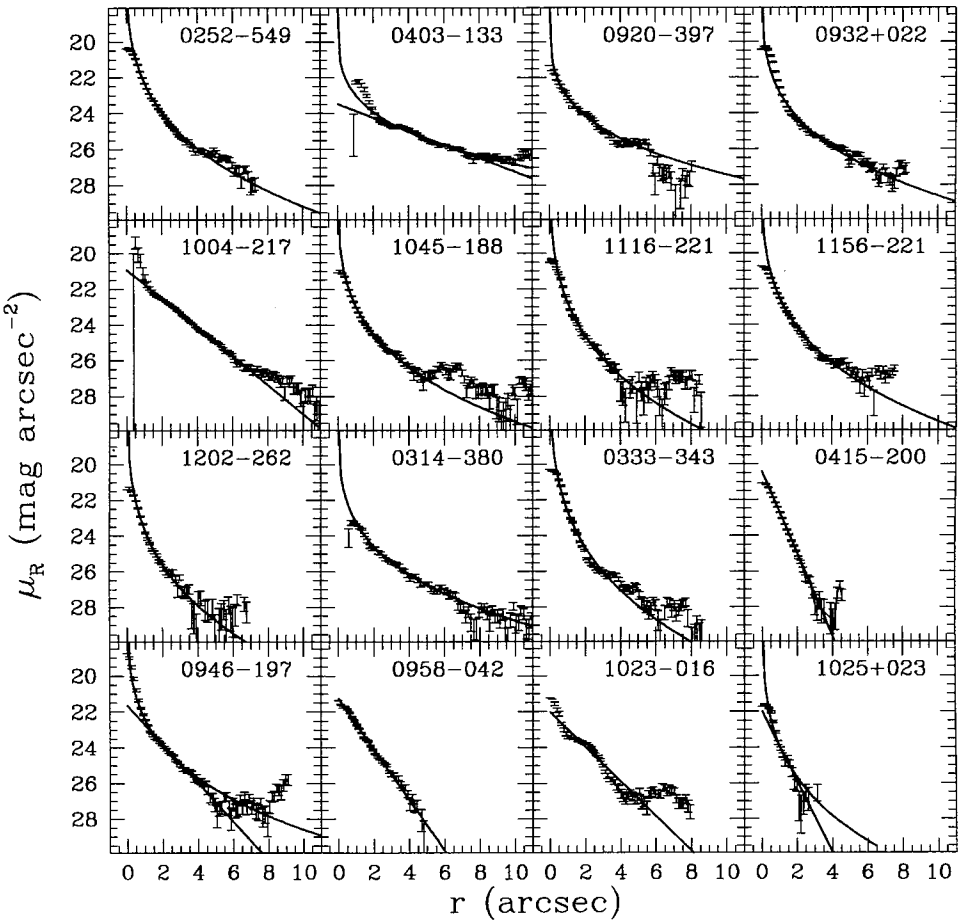


**Figure 6.** Azimuthally averaged luminosity profiles of the residual images shown in Figs 4(a) and (b). The error bars show the $1\sigma$ deviation. Full drawn lines show the profiles of the best fit. Both the $r^{1/4}$ and exponential disc profile are shown for uncertain cases.

RLQs are more compact than normal low-redshift ellipticals, also holds for our data. The fact that the seeing results in systematically underestimated scalesizes (cf. Section 4.4) could reduce this effect. The exact amount of this should be examined in more detail before we can conclude anything, however. For the object in common between our study and that of Romanishin & Hintzen, PKS 0932 + 022, we derive the same effective radius and magnitude of the elliptical host galaxy, within the errors.

The *V*–*R* colours of the hosts, which were observed in several bands, are plotted in Fig. 7. The colours of the template stellar populations shown in the figure were derived by integrating the redshifted filter profile convolved with spectral energy distributions adopted from Coleman et al. (1980). The colours were corrected for the different CCD quantum efficiencies in *V* and *R*. Although the errors are quite large, $\sim 0.2$ mag, it is apparent that the colours on the whole are typical for present-day late-type discs and irregular galaxies. It is remarkable that three of these hosts appear to have elliptical luminosity profiles.

We cannot completely rule out the possibility that the blue colours are due to a mixture of stellar light and scattered QSO light. If the stellar populations in the galaxies classified as E types are in fact those of normal late-type galaxies, and our colours are representative, we can estimate the fraction of scattered light from the QSO, in the

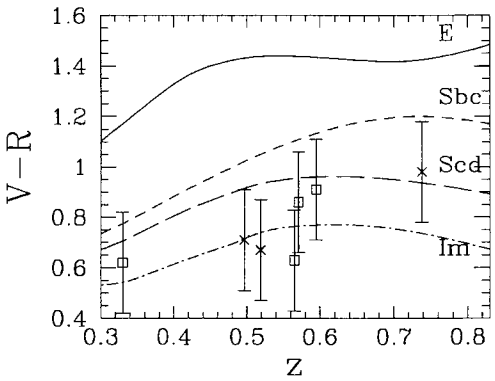


**Figure 7.** The *V*–*R* colour as a function of redshift for non-evolving E (full line), Sbc (dashed), Scd (long dashed) and Im (dot-dashed) galaxies. Squares and crosses mark the positions of radio-loud and radio-quiet quasar host galaxies, respectively.

case of electron scattering. Assuming that $M_R = -24.0$ and $V-R=0$ for a typical QSO, $V-R=1.4$ for an E galaxy and $M_R = -22.2$ and $V-R=0.8$ for the host object, we find that as much as $\sim 10$ per cent of the light of the QSO may be scattered. The contribution of the scattered light to the image of the host galaxy may then be of order 50 per cent or more. In this example, the scattered component has $M_R = -21.6$ while the stellar component has $M_R = -21.2$.

This could explain why elliptical host galaxies, as first noted by Romanishin & Hintzen (1989), at a given effective radius are more luminous than normal E galaxies (Romanishin 1986). A more probable situation, however, is that the scattering agent is dust. In that case it is difficult to calculate the fraction of scattered light as a function of the wavelength because it is dependent on the properties (size and composition) of the dust.

Apparent nearby QSO companion objects are a common feature. Table 3 includes the distances and rough $R$ magnitudes (measured in circular apertures) of the nearest companions. Because the redshift of the companions is unknown, we are not able to tell whether they are physically associated with the QSO host galaxy. All companion objects have fainter magnitudes than the host galaxy we associated them with. More complete companion statistics will be discussed in a future paper.

It has been speculated that there exist 'naked' quasars (Bahcall et al. 1995) without any companion host galaxy. Our data include at least two such possible cases, PKS $0928+008$ and PKS $1143-287$, both radio-loud. However, the simulation made in Section 4.4 indicates that we cannot retrieve galaxies fainter than about $M \sim -20$ mag. Another possibility is that the host is an extended disc of very low surface-brightness. The classical low surface-brightness disc, Malin 1 (Bothun et al. 1987), does have an active nucleus, albeit of low luminosity. Its central surface-brightness in $V$ is only 25.7 mag arcsec$^{-2}$, but still the absolute magnitude is $M_V \sim -21$, because it is so extended. Since cosmic dimming at $z > 0.4$ is $> 1.5$ mag arcsec$^{-2}$, a Malin 1 type disc would not be detected at the redshift of the quasars in this study.

## 6 SUMMARY

We have found host galaxies in about 70 per cent of the observed radio-loud and radio-quiet quasars. In two cases where no host was found, the limiting $M_R \sim -20$. The detected host galaxies are generally relatively big, bright and blue. Radio-loud quasars are typically found in elliptical galaxies with absolute $R$ magnitude $\sim -22.3$, and effective radii of 4 kpc. Exceptions to this rule are found, however, i.e. the host of the radio-loud quasar PKS $1004-217$ seems to be a disc galaxy in a merger state with a smaller companion. Hosts of radio-quiet quasars are typically large discs or ellipticals with scalelengths of several kpc and $R$ magnitudes $\sim -22.0$. The colours of the stellar populations in both types of hosts are typical for late-type spirals and irregulars. Close companion galaxies of fainter magnitudes are common. In the best-resolved hosts we detect tidal arms, indicating recent galaxy–galaxy interaction/merger. We conclude that the quasar phenomenon at $0.4 < z < 0.8$ in general takes place in galaxies of large dimensions, probably in a state of interaction with smaller companions.

## ACKNOWLEDGMENTS

We thank the staff at ESO for the excellent way in which the remote observing was performed. In particular, night assistant Vincente Reyes is thanked for his excellent assistance and for allowing us to turn off his salsa music every once in a while. Leon Lucy is thanked for pointing out a number of important references. We are indebted to Richard Hook for providing and explaining the codes for the image restoration program and the PSF generation code. We made use of the NASA/IPAC Extragalactic Database (NED) which is operated by the Jet Propulsion Laboratory, CALTECH, under contract with the National Aeronautics and Space Administration. This research was partly supported by a grant from the Swedish Research Council.

## REFERENCES

Bahcall J. N., Kirhakos S., Schneider D. P., 1995, ApJ, 450, 486
Bessel M. S., 1979, PASP, 91, 589
Bothun G., Impey C., Malin D., Mould J., 1987, AJ, 94, 23
Burstein D., Heiles C., 1982, AJ, 87, 1165
Coleman G. D., Wu C. C., Weedman D. W., 1980, ApJS, 43, 393
Disney M. J. et al., 1995, Nat, 376, 150
Dunlop J. S., Taylor G. L., Hughes D. H., Robson E. I., 1993, MNRAS, 264, 455
Ellingson E., Yee H. K. C., Green R. F., 1991, ApJ, 371, 49
Graham J. A., 1982, PASP, 94, 244
Griffith M. R., Wright A. E., Burke B. F., Ekers R. D., 1994, ApJS, 90, 179
Griffith M. R., Wright A. E., Burke B. F., Ekers R. D., 1995, ApJS, 97, 347
Hewitt A., Burbidge G., 1993, ApJS, 87, 451
Hook R. N., Lucy L. B., Stockton A., Ridgway S., 1994, ST-ECF Newsletter, 21, 16
Hook R. N., Lucy L. B., 1994, in Hanisch R. J., White R. L., eds, Proc. the Restoration of HST Images and Spectra.. STScI, p. 86
Hutchings J. B., 1995, AJ, 110, 994
Hutchings J. B., Morris S. C., 1995, AJ, 109, 1541
Hutchings J. B., Neff S. G., 1992, AJ, 104, 1
Hutchings J. B., Janson T., Neff S. G., 1989, ApJ, 342, 660
Hutchings J. B., Crampton D., Johnson A., 1995, AJ, 109, 73
Lowenthal J. D., Heckman T. M., Lehnert M. D., Elias J. H., 1995, ApJ, 440, 588
Lucy L. B., 1994, in Hanisch R. J., White R. L., eds, Proc. the Restoration of HST Images and Spectra. STScI, p. 79
MacKenty J. W., 1990, ApJS, 72, 231
Maraziti D., Stockton A., 1994, PASP, 106, 71
McLeod K. K., Rieke G. H., 1994a, ApJ, 420, 50
McLeod K. K., Rieke G. H., 1994b, ApJ, 431, 137
Robson I., Dunlop J., Taylor G., Hughes D., 1995, BAAS, 187, 87.03
Romanishin W., 1986, AJ, 91, 76
Romanishin W., Hintzen P., 1989, ApJ, 341, 41
Saglia R. P., Bertschinger E., Baggley G., Burstein D., Colless M., Davies R. L., McMahan R. K., Wegner G., 1994, MNRAS, 264, 961
Sanders D. B., Soifer B. T., Elias J. H., Madore B. F., Matthews K., Neugebauer G., Scoville N. Z., 1988, ApJ, 325, 74
Smith E. P., Heckman T. M., Bothun G. D., Romanishin W., Balick B., 1986, ApJ, 306, 64
Stockton A., MacKenty J. W., 1987, ApJ, 316, 584
Turner J. A., Phillipps S., Davies, J. I., Disney M. J., 1993, MNRAS, 261, 39
Véron-Cetty M. P., Woltjer L., 1990, A&A, 236, 69
Véron-Cetty M. P., Véron P., 1993, ESO Sci. Rep. 13
Wade R. A., Hoessel J. G., Elias J. H., Huchra J. P., 1979, PASP, 91, 35
Wilson A. S., Colbert E. J. M., 1995, ApJ, 438, 62
Wright A. E., Griffith M. R., Burke B. F., Ekers R. D., 1994, ApJS, 91, 111

## APPENDIX A: NOTES ON SELECTED INDIVIDUAL OBJECTS

**PKS 0252 – 549, radio loud** ($z = 0.537$) The host in this object is embedded in a faint halo, of surface brightness $\sim 26$ mag arcsec$^{-2}$ in $R$ (a level not seen in the contour plot), which is elongated in the direction of a companion object located 44 kpc SW of the host. The extension of the halo is about 50 kpc. Within this halo several fainter objects are located. The halo could be the stellar debris from the interaction with the companion, which is nearly as bright as the host galaxy.

**0314 – 380, radio quiet** ($z = 0.484$) The QSO image, one of the brightest in our sample, was saturated in a few central pixels. It also has very faint stellar spikes which are not equally bright in the star used to generate the PSF. This resulted in artificial structures in the QSO-subtracted image. Thus, the SW and SE 'arms' seen in the contour plots are not real.

**0333 – 343, radio quiet** ($z = 0.621$) **and 0342 – 250 radio quiet** ($z = 0.653$) For these objects we do not detect any significant residual flux in the $V$ images.

**PKS 0403 – 133, radio loud** ($z = 0.571$) An arm structure (either a tidal or a spiral arm) is seen stretching towards two nearby companions about 50 kpc from the centre. The best fit to the luminosity profile of the host is an exponential disc (particularly in the $V$ image of the host), although this is a radio-loud quasar. A second nucleus is seen about 5 kpc SW of the centre.

**0414 – 060, radio loud** ($z = 0.781$) Although we do not detect any host object in this QSO, the faint nebulosity to the north of the QSO image (see Fig. 4a) could possibly be due to a host or companion object.

**MC 0415 – 200, radio quiet** ($z = 0.604$) A nearby companion with $M_R = -19.4$ at a projected distance of about 17 kpc is located to the east of the host galaxy.

**PKS 0920 – 397, radio loud** ($z = 0.591$) This system appears to be interacting with the south-east companion 15 kpc from the centre of the host galaxy.

**PKS 0928 + 008, radio loud** ($z = 0.505$) After subtraction of the PSF from the QSO image only background noise remains. The limiting magnitude is thus $M_R \sim -20.10$.

**PKS 0932 + 022, radio loud** ($z = 0.652$) An arm structure resembling a tidal tail stretches out to the north of this object. The luminosity profile is a clear $r^{1/4}$ law. This object has been observed previously by Romanishin & Hintzen (1989). They derive an effective radius within $1\sigma$ of our estimate. Our host galaxy magnitude is $\sim 0.4$ brighter than theirs, however. It should be noted that their integration time in $R$ was only half of the one we used and that their FWHM was twice as large.

**MC 0946 – 197, radio quiet** ($z = 0.519$) This object is located in a compact group of galaxies with at least 8 components within a projected distance of 150 kpc.

**PKS 0958 – 042, radio quiet** ($z = 0.497$) A companion is located 8 kpc from the centre of the host galaxy to the

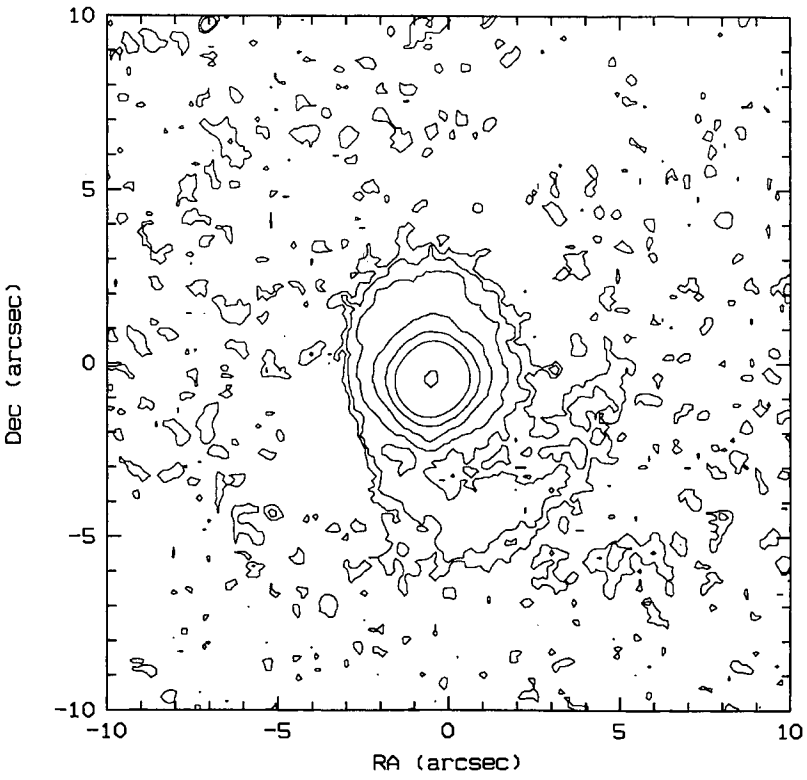


**Figure A1.**

north-east. This object is possibly in the process of merging with the host. We were unable to measure its magnitude.

**PKS 1004 – 217, radio loud** ($z = 0.33$) This QSO was included to facilitate a comparison of our data with previous studies. Comparing our data with the images in Véron-Cetty & Woltjer (1990), it is clear that the present data is of much higher quality. In fact, we can resolve an extended tidal arm in this galaxy. Fig. A1 shows the result of the subtraction of a model disc (with structural parameters as derived from the best fit) from the host galaxy image. An extended tidal arm, splitting up into two components at the tail, is seen. It is likely that this is the result of a merger with a fainter galaxy, $R_{\rm arm} \sim 21.5$. The material falling towards the centre of the host could be the fuel powering the QSO.

**1016 – 028, radio quiet** ($z = 0.717$) No apparent host galaxy is seen in this object. Only one relatively faint star was used to generate the PSF image, and it appears that its profile is somewhat different from the profile of the QSO, resulting in a relatively large residual flux after the PSF subtraction. For this reason we do not present a limiting magnitude. This objects appears to be a member of a group of galaxies lined up in a chain to the east of the QSO.

**1023 – 016, radio quiet** ($z = 0.738$) The host galaxy resembles a grand design spiral galaxy with two arms connected with two nearby satellite objects. A central bar is traced, although the centre is not well resolved.

**PKS 1143 – 287, radio loud** ($z = 0.45$) No host galaxy is detected at the limit of the observations, $M_R \sim -19.83$.